JGR Atmospheres

RESEARCH ARTICLE
10.1029/2024JD042972

Multiscale WRF Modeling of Meso- to Micro-Scale Flows During Sundowner Events

Andrew Janiszeski[1] and **Paola Crippa**[1]

[1]Department of Civil and Environmental Engineering and Earth Sciences, University of Notre Dame, Notre Dame, IN, USA

Key Points:

- The highest model resolution coupled with high-resolution topography data produces the most realistically structured Sundowner
- The multiscale drivers of Sundowners are: increased mountaintop stability and mountain wave activity within near-surface critical layers
- Downslope winds ascend over coastal adiabatic layers exhibiting turbulence atop them with reverse flow beneath

Supporting Information:

Supporting Information may be found in the online version of this article.

Correspondence to:

A. Janiszeski,
ajanisz2@nd.edu

Citation:

Janiszeski, A., & Crippa, P. (2025). Multiscale WRF modeling of meso- to micro-scale flows during Sundowner events. *Journal of Geophysical Research: Atmospheres*, *130*, e2024JD042972. https://doi.org/10.1029/2024JD042972

Received 14 NOV 2024
Accepted 24 JAN 2025

Abstract Two Sundowner events observed during the Sundowner Wind Experiment (SWEX) project are analyzed using a realistically forced large eddy simulation (LES) employing a multiscale Weather and Research Forecasting (WRF) model configuration with domain grid spacings ranging from 11,250 to 30 m centered over the Santa Barbara, CA region to examine their meso- to micro-scale drivers. The main drivers of both events are increasing mountaintop stability and the mountain wave activity exhibiting a hydraulic jump and near-surface critical layer. Another important finding is ascent of the downslope flows over the turbulent adiabatic layers at the coastal regions. In both events, the strong downslope flow warms and dries the air descending the southern slopes of the SYM adiabatically generating a deepening adiabatic layer that is 0.4 to as much as 1 km deep during peak Sundowner intensity over the coastal regions. This layer, exhibiting turbulence within and atop, is characterized with the strong downslope flow atop with much weaker, and at times, reversed flow beneath over the coastal regions. This flow structure, along with regions of turbulence within and atop the adiabatic layer, is indicative of a mountain lee-wave rotor. Coastal locations in both events remain relatively unaffected. Further investigations are needed to determine whether or not this is consistent across all Sundowner events observed during the SWEX project and whether turbulence helps diffuse or accelerate the flows.

Plain Language Summary In coastal Southern California near Santa Barbara, most commonly beginning in late afternoon or evening in spring and summer, frequent downslope flows, called Sundowners, occur as northerly winds accelerate down the southern slopes of the Santa Ynez Mountains (SYM) into the Santa Barbara region. These downslope wind events pose a risk to public safety as they are commonly linked with spread of wildfires into a densely populated region, and therefore, understanding their causes and evolution are critical. This study examines, using a novel modeling approach with the Weather Research and Forecasting model coupled with high-resolution topography data, to understand the meso- to micro-scale drivers of such events and examine the details of such flows over complex terrain beyond what previous research has done. Our findings indicate that the complex interaction of increasing atmospheric stability atop the SYM after sunset along with mountain wave dynamics and a subsequent change to atmospheric stability downwind of the SYM result in turbulent downslope flows with large spatiotemporal variability tied to the complex SYM terrain.

1. Introduction

In coastal Southern California near Santa Barbara (SB), most commonly beginning in late afternoon or evening in spring and summer, frequent downslope flows, called Sundowners, occur as northerly winds accelerate down the southern slopes of the Santa Ynez Mountains (SYM) into the SB region (Blier, 1998; Ryan, 1996). These downslope flows are linked with the spread of many wildfires, which pose a serious public safety concern to the region (Cannon et al., 2017; Carvalho et al., 2020; Fovell & Gallagher, 2018; Kolden & Abatzoglou, 2018; Zigner et al., 2020, 2022).

Previous studies of Sundowners have documented the presence of frequent wind gusts over 20 m s^{-1} with such events characterized by a strong cross-mountaintop flow that is directed downward along the southern SYM slopes after sunset via mountain waves caused by increased stability atop the SYM (Carvalho et al., 2020, 2024; Hatchett et al., 2018). Three different types of Sundowners are defined in previous literature (Jones et al., 2021). Western Sundowners have maximum downslope flows over the western SYM range within a north to northwest synoptic flow, whereas eastern Sundowners have stronger downslope flows over the eastern SYM range within a north to northeast synoptic flow. Both types of Sundowners may occur simultaneously or independently in a "hybrid" event (Carvalho et al., 2024).

Mountain downslope wind dynamics in various high elevation alpine regions have been studied over the past few decades (Durran, 1990, 2003; Durran & Klemp, 1987; Gallus & Klemp, 2000; Grubišić & Billings, 2007, 2008; Jiang & Doyle, 2008; Klemp & Lilly, 1975; Lawson & Horel, 2015; Smith, 1985). However, as noted by Carvalho et al. (2020), the complex geography of the region, including the proximity of the Santa Ynez Mountains to the Pacific Ocean, results in a combination of the downslope flows from mountain wave activity interacting with a cool stable marine boundary layer over the Pacific Ocean. Only a few studies have attempted to understand the interaction of these two features and have had limited success using high resolution numerical mesoscale modeling (Cannon et al., 2017; Carvalho et al., 2020; Smith et al., 2018). Cannon et al. (2017) simulated an 11-day period featuring multiple Sundowners using the Weather Research and Forecasting (WRF) model and compared output to observations. Their study showed that using WRF with 2 km grid spacing the temperature, pressure, and wind directions were captured while wind speeds were under forecast and the marine boundary layer was poorly captured resulting in inaccurate simulated flows near the SB coastal region. Previous observational studies, such as Blier (1998), noted the importance of a strong offshore flow in eroding the stable marine boundary layer and allowing for the Sundowner events to occur in the SB region.

The main focus of several modeling studies has been examining the large spatiotemporal variability of meso- to micro-scale atmospheric boundary layer (ABL) flows over steep terrain where mountain slopes, canyons, and land surface type impact the flows making them difficult to simulate (Carvalho et al., 2020, 2024; Daniels et al., 2016; Duine et al., 2019; Lundquist et al., 2010). Until recently, simulations of such flows were performed with model grid spacings on the order of ∼1 km or greater, which presents challenges and limitations for properly simulating and elucidating the multiscale dynamical drivers of such flows. Also, the lack of frequent observations of such phenomena has made model validations and understanding dynamical causes difficult. A novel alternative approach using realistically forced large eddy simulation (LES), which incorporates high-resolution topography, land use, and lateral boundary conditions from lower resolution numerical weather models, has been used to explicitly resolve important processes that influence ABL flows (Haupt et al., 2019; Talbot et al., 2012). A recent study by Giani and Crippa (2024), using this approach, tested multiscale modeling sensitivity to different WRF turbulence schemes, initial and lateral boundary conditions, and land use and terrain characterization over complex terrain in Portugal. Their experiments used a multiscale WRF model domain configuration, also referred to as realistically forced LES, with grid spacing ranging from 11,250 m in the outer-most domain to 30 m in the innermost. This configuration allowed for dynamically downscaling atmospheric flows to the subgrid-scale (SGS) model resolutions while explicitly resolving turbulence and other ABL processes related with land-surface type, topography, and buoyancy. Their study demonstrated the capability of WRF to simulate micro- to meso-scale flows in complex terrain providing a framework to be used in other regions where complex ABL flows are found.

In order to investigate the dynamics, spatiotemporal variability, and role of ABL processes in Sundowners, the research presented herein uses the new multiscale WRF model approach similar to Giani and Crippa (2024) to simulate meso- to micro-scale ABL flows during two selected Sundowner events from the 1 April to 15 May 2022 Sundowner Wind Experiment (SWEX) Project, a project designed investigate the ABL structure and dynamics of Sundowners including: mountain waves, stability, critical layers, and the role of topography in such events (Carvalho et al., 2024). This approach to simulating such flows is unique in that it is the first attempt to simulate Sundowners using a realistically forced LES that incorporates high resolution topography data and allows for an investigation into the roles of turbulence and complex terrain on Sundowners beyond previous work. Two separate Sundowner events observed during SWEX are used: an eastern Sundowner event on 4–5 April 2022 and a western Sundowner event on 8–9 May 2022. These two events are chosen to deepen the understanding of the multiscale drivers of Sundowner events by individually examining and comparing the drivers of both eastern and western Sundowner type events in an effort to determine how similar drivers are for both Sundowner types. The goals of this research are: (a) to determine and elucidate the multiscale drivers and influences of Sundowner events such as mountain waves, stability, turbulence, and marine boundary layer interaction beyond previous research, (b) to highlight the importance of microscale WRF modeling in capturing the complex ABL flows coupled to high resolution terrain, and (c) to quantify WRF skills at different resolutions in capturing Sundowners against a range of SWEX observations. The paper is organized as follows; Section 2 discusses the synoptic backgrounds, WRF model configurations, and metrics used for evaluating WRF model performance for both events. Section 3 discusses the results of the simulations of both events including WRF model prediction skill and

determining the meso- to micro-scale features and drivers of both events. Section 3 also examines turbulence and ABL characteristics near the coastal regions, and Section 4 summarizes key findings and concludes the paper:

2. Simulated Sundowner Events

2.1. Synoptic Background of 4–5 April and 8–9 May 2022 Sundowner Events

Both Sundowner events occurred under favorable synoptic conditions for such an event with a ridge of high pressure, especially in the lower troposphere, over the Pacific, well offshore of the Pacific Coast and troughing further inland. This resulted in a low-level northwesterly to northerly flow, which is favorable for downslope winds on the southern slopes of the SYM.

The 4–5 April 2022 Sundowner event, the first intensive operation period (IOP) or IOP 1 of the SWEX Project, impacted the eastern SYM range and the nearby Montecito, CA region with its peak intensity between 0300 and 0900 UTC 5 April 2022. The synoptic pattern during the Sundowner event indicates a ridge of high pressure at both 500 hPa (Figure S1a in Supporting Information S1) and 850 hPa (Figure S1b in Supporting Information S1) located over the eastern Pacific Ocean well offshore of Southern California and a weak mid-level trough over the U.S. Desert Southwest and extending into northern Mexico. This resulted in a northerly low-level flow of 25–30 m s^{-1} at 850 hPa over coastal Southern California crossing the long axis of the SYM and providing for ideal conditions for an eastern Sundowner type event. Meanwhile, the 8–9 May 2022 Sundowner, IOP 8 of the SWEX Project, impacted the western SYM range mostly at and west of SB. A deep 500 hPa trough with a strong 60 kt (30 m s^{-1}) west-northwesterly flow was present over Southern California (Figure S1c in Supporting Information S1). At 850 hPa, a northwesterly flow of 20–25 kts (10–15 m s^{-1}) was found over the SB region in between an offshore ridge and trough over the Intermountain West (Figure S1d in Supporting Information S1).

2.2. WRF Model Configuration

To analyze the Sundowner events, we used WRF v4.5 in a multiscale configuration with five one-way nested domains (d01–d05) centered over the SB area with domain grid spacings spanning of 11,250 to 30 m (Figures 1a–1f) (Skamarock et al., 2021). The complex topography of the region especially the steep slopes of the SYM posed a challenge to simulating flows within the high-resolution inner-most domains, especially d05. For both events, the inner-most domain, d05, with 30 m grid spacing was situated on the southern slopes of the SYM instead of extending over the crest of the SYM to alleviate numerical instabilities caused by the steepest slopes (see Figures 1c and 1f).

The three outermost domains (d01, d02, and d03) had 77 vertical eta levels reaching a constant isobaric surface of 50 hPa at the model top using the new hybrid coordinates of the ARW solver (Beck et al., 2020). The model vertical eta levels were chosen to have nearly geometrically increasing Δz in an idealized ABL, starting from $\Delta z = 36$ m at the surface and reached an approximately constant $\Delta z = 350$ m above the ABL similarly to what used by Giani et al. (2022) and Giani and Crippa (2024). For the IOP 1 simulation, consistent with other previous multiscale simulations (Giani & Crippa, 2024; Giani et al., 2022; Ronda et al., 2017), we increased the vertical levels in d04 and d05 to 91 levels and 109 levels, respectively, to better resolve the ABL with finer horizontal grid spacings of 150 m in d04 and 30 m in d05. We chose $\Delta z = 24$ m in d04 and $\Delta z = 12$ m in d05 in the ABL and $\Delta z \approx 80$ m atop the ABL in the free atmosphere. Since IOP 8 had stronger winds and subsequently more turbulent flow with stronger updrafts and downdrafts, d04 and d05 had the same 77 verticals levels as the other domains in order to prevent numerical instability over the steep SYM slopes.

The simulations employed the traditional Yonsei University (YSU) 1D Planetary Boundary Layer scheme for the d01–d03 domains (Hong et al., 2006). In order to resolve TKE in the LES scale domains, d04 and d05, we use the Deardorff (1980) TKE closure. More details regarding the TKE closure scheme can be found by Skamarock et al. (2021). Previous studies (e.g., De Moliner et al., 2024; Giani & Crippa, 2024; Giani et al., 2022) have also highlighted the importance of high-resolution topography data in simulating meso-microscale flows through complex terrain. For this model simulation, the two outer-most domains (d01 and d02) used the WRF Preprocessing System (WPS) default static topography data, the Global Multi-resolution Terrain Elevation Data 2010 (GMTED) from the U.S. Geological Survey (USGS), with a resolution of ~900 m, and Noah-modified 21-category land cover data from the International Geosphere Biosphere Programme Moderate Resolution Imaging Spectroradiometer (IGBP-MODIS). For the three inner-most domains we used the same land use data, but for

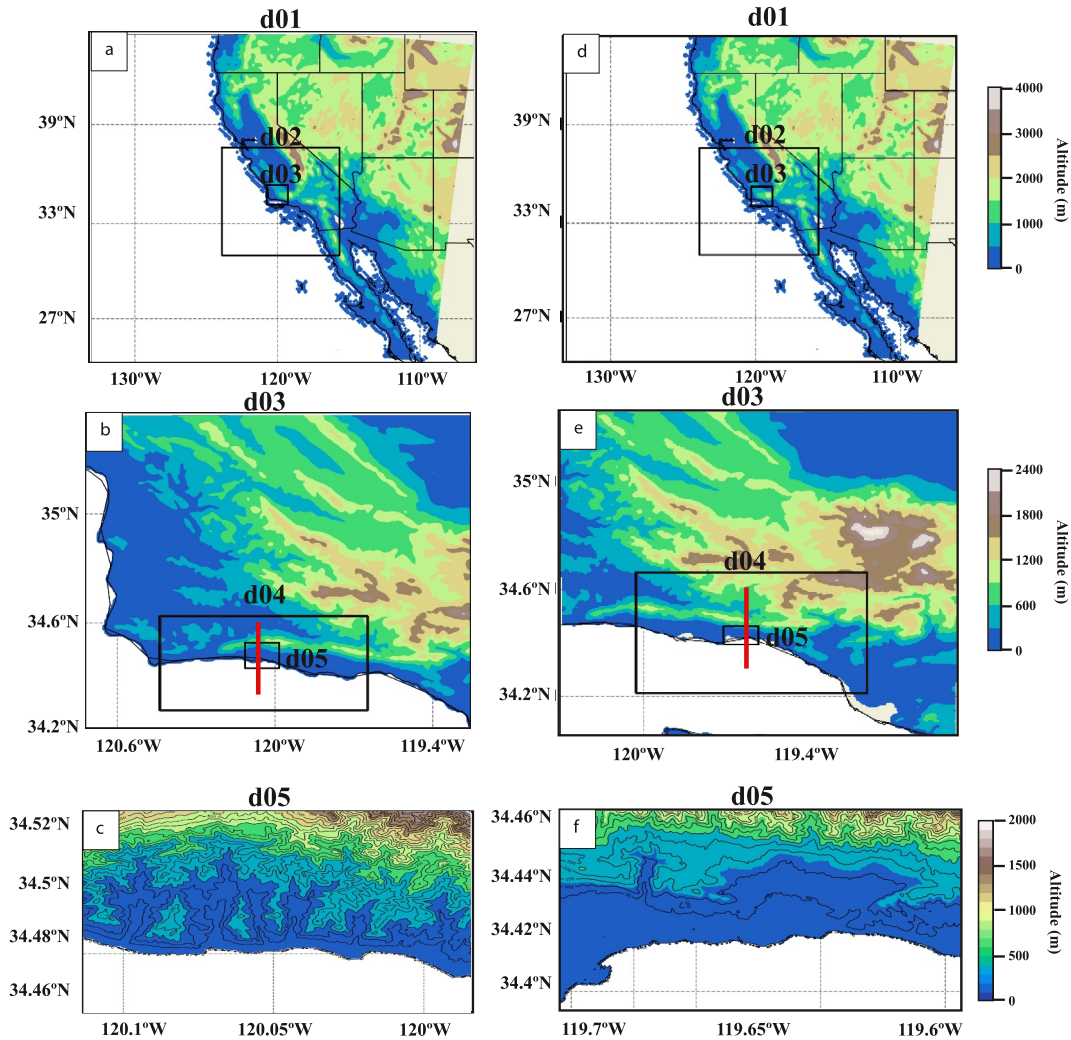

Figure 1. Nested configuration of WRF model domains for IOP 8 (first column) and IOP 1 (second column). The d01 grid spacing is 11,250 m, d02 is 3,375 m, d03 is 750 m, d04 is 150 m, and d05 is 30 m. Cross sections used for analysis are drawn in red in (b) and (e) and the color shading indicates elevation (m).

topography, we used 30 m resolution topography data from the Shuttle Radar Topography Mission (SRTM) (Werner, 2001). The European Centre for Medium-Range Weather Forecasts Reanalysis v5 (ERA5) (European Centre for Medium-Range Weather Forecasts, 2019) data were used for the initial and lateral boundary conditions of the simulation with ~28 km spatial resolution and hourly update frequency (Hersbach et al., 2020), which allows for greater sensitivity to changing synoptic conditions which may affect the meso–micro-scale ABL Sundowner flows. The simulations were run from 1800 UTC 3 April 2022 to 1800 UTC 5 April 2022 for IOP 1 and 1800 UTC 7 May 2022 to 1800 UTC 9 May 2022 for IOP 8, allowing for over 24 hr of spin up time before each event occurred, which is consistent with previous WRF studies. WRF model output frequency is 60, 60, 30, 5, and 5 min for domains d01, d02, d03, d04, and d05 respectively. Instantaneous model output at the locations of the ISFS towers corresponds to the model time step for each domain and is 75, 25, 5, 1, and 0.2 s for domains d01, d02, d03, d04, and d05, respectively.

2.3. Data and Metrics Used to Evaluate Model Performance

In this section, we introduce the observational data and statistical metrics used to quantify model performance of simulated 10 m winds across the d01–d05 domains and the indicators used to quantify and describe mountain wave patterns for both Sundowner events.

Relevant to evaluating the model performance are the 5 min averaged 10 m horizontal wind speeds measured by the NCAR ISFS flux towers during both events (NSF NCAR-Earth Observing Labratory, 1990; Sun et al., 2003). The ISFS towers are spread across the SYM region with several towers (12, 7, 8, 9, 10, and 11) along the SYM, whereas others (1, 6, 5, 3, 18, and 4) are located along either the SYM slopes or in the coastal region. Several towers (13, 14, 15, and 16) are located upstream of the SYM (Figure S2 in Supporting Information S1). ISFS tower 17 is omitted from the analysis because it was not located near the SYM. No ISFS towers are located in the d05 domain for IOP 1 event so no d05 comparison is shown. We compute the indicators of Root-Mean-Square-Error (RMSE) and Mean Bias (MB) as follows:

$$\mathrm{RMSE} = \left(\frac{1}{N} \sum_{t=1}^{N} \left(\overline{W_m}(t) - \overline{W_O}(t) \right)^2 \right)^{0.5} \tag{1}$$

$$\mathrm{MB} = \frac{1}{N} \sum_{t=1}^{N} \left(\overline{W_m}(t) - \overline{W_O}(t) \right) \tag{2}$$

where W_m is the 5-min sites-averaged modeled wind speed, W_O is the 5-min observed sites average wind speed, t is the time coordinate, and N is the number of observations. The statistics are computed over entire 48-hr simulation period. Three ISFS tower versus modeled wind timeseries are compared to characterize the temporal evolution of the Sundowners at both the SYM crest and adjacent regions along the southern SYM slopes and nearby coastline (Figure 2).

To quantify the presence of critical layers associated with mountain wave activity, we calculate the gradient Richardson number (R_i):

$$R_i = \frac{g}{\Theta} \frac{\left(\frac{d\Theta}{dz} \right)}{\left(\frac{du}{dz} \right)^2 + \left(\frac{dv}{dz} \right)^2} \tag{3}$$

where g is gravity (m s^{-2}), $d\Theta/dz$, du/dz, and dv/dz are the vertical gradients of potential temperature (K), zonal, and meridional wind speeds between model vertical levels (dz), respectively. The gradient Richardson number, within a thin layer (small dz), relates the buoyant consumption of turbulence with the shear production of turbulence. Previous research (Cannon et al., 2017; Durran, 1990) has highlighted the collocation of $R_i < 0.25$, signifying a dynamically unstable flow within a critical layer in which turbulence can reflect mountain wave energy and augment the downslope flows.

We also calculate the Froude number (F_r), which represents the ratio of interial to gravitational acceleration for a fluid:

$$F_r = \frac{v}{\sqrt{gd}} \tag{4}$$

where v is the v component of the wind (m s^{-1}) which is parallel to the cross sections F_r is calculated along, g is gravity (m s^{-2}), and d is depth of a layer between two model vertical levels. In both cases, d is very small (either 24 or 36 m in d04 domain) in the boundary layer, which gives similar thermal and dynamic characteristics to air within each layer which is critical for F_r calculations of such ABL flows. In the context of mountain waves, a transition from $F_r > 1$ (supercritical flow) to $F_r < 1$ (subcritical flow) signifies a hydraulic jump, which is observed in various downslope flow regimes (Cao & Fovell, 2016; Durran, 1990).

3. Results

3.1. Evaluation of WRF Skills in Simulating Sundowner Events

In this section, we describe the WRF model skill in simulating wind speeds across all the domains, when possible, at the ISFS towers during each Sundowner event. Tables S2 and S3 in Supporting Information S1 summarize the indicators across IOPs 1 and 8, respectively.

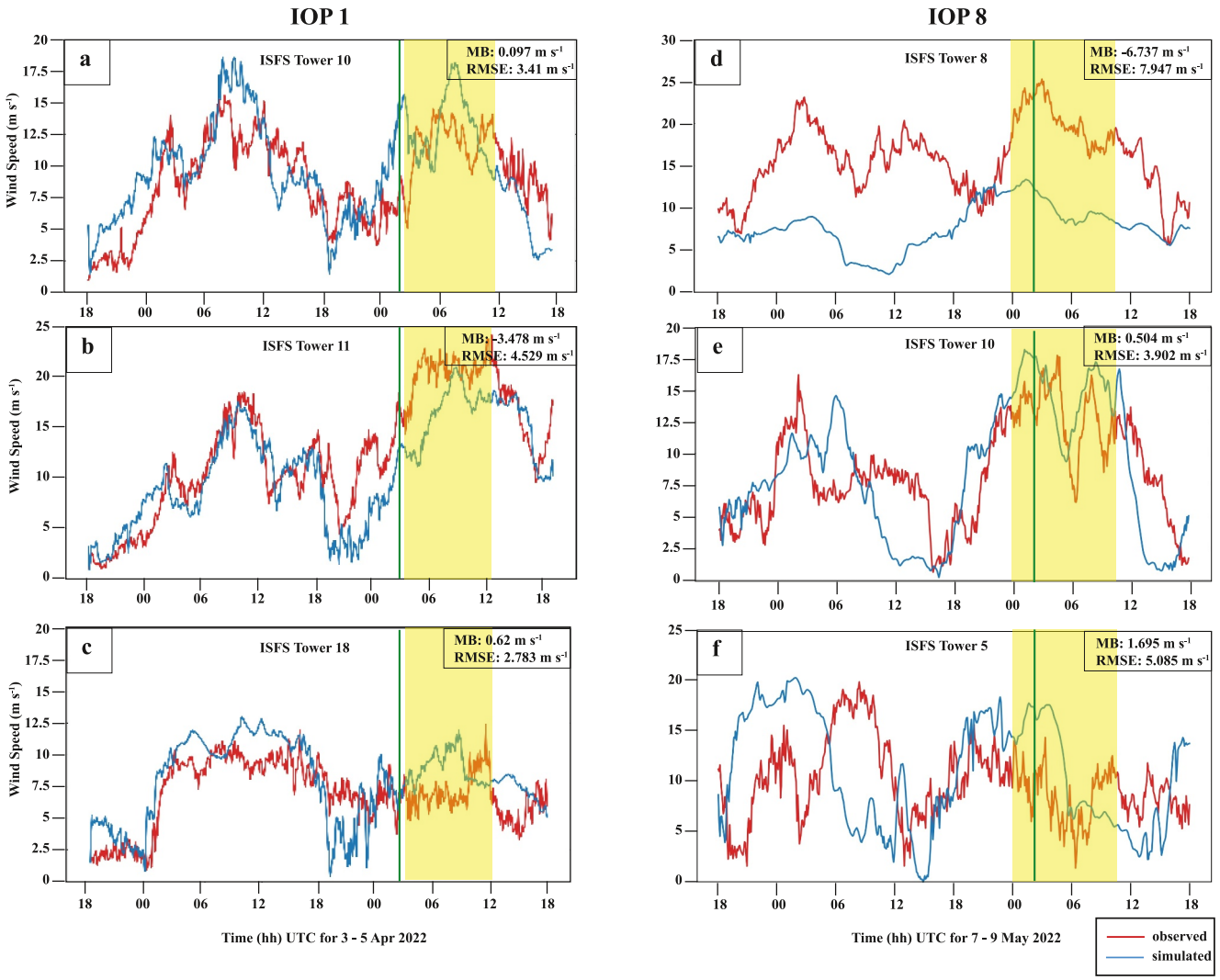

Figure 2. Timeseries of ISFS tower observed 10 m winds (m s^{-1}) versus WRF simulated 10 m winds (m s^{-1}) for (a–c) three different ISFS towers in IOP 1 and (d–f) three different towers in IOP 8. Yellow shaded regions denote times of interest and green vertical line denotes sunset time.

In general, winds are overpredicted for most sites in both cases. With the exception of a few locations, such as tower 8 in both IOPs and towers 9 and 16 in IOP 1 with MBs of ∼−7 to −9 m s^{-1} signifying a large under-prediction of the flow, MBs are generally between 0 and 5 m s^{-1} for both IOPs. RMSE values are typically between 2 and 7 m s^{-1} for most towers at all resolutions. The larger RMSE values are generally found across all resolutions at towers 8 and 9 for IOP 1 and at towers 1, 6, and 8 for IOP 8 (Tables S2 and S3 in Supporting Information S1). MB and RMSE values varied mostly between towers along the SYM crest while in coastal regions; generally, RMSE and MB values are more consistent between towers indicating that the model had prediction errors, the flows are more consistently simulated and less erratic, likely owing to more homogenous terrain of the coastal areas compared with the sharp SYM crest. The median MBs and RMSEs for IOP1 across all sites, for resolutions d01–d04, are between 0.3585–1.216 m s^{-1} and 3.786–4.698 m s^{-1}, respectively (Table S2 in Supporting Information S1). Similar results are found for IOP8 where the median MBs and RMSEs across all sites, for resolutions d01–d05, vary between 2.003 and 2.931 m s^{-1} and 3.786–4.698 m s^{-1}, respectively (Table S3 in Supporting Information S1). These values indicate that increasing resolution does not necessarily improve predicted wind speed accuracy. However, despite no notable statistical improvement of point prediction accuracy as resolution increases, the domains with coarser grid spacing, d01 and d02, do not properly resolve the local terrain and produce winds that are not representative of the actual Sundowner dynamics. This suggests that point-based statistical metrics are not representative of the actual model's ability to capture the occurrence and evolution

of these events, whereas an integrated assessment that analyzes dynamic features of the flow is critical. The inner domains, d03–d05, represent better the steep SYM terrain and subsequently capture the actual dynamics of the Sundowners providing for a more accurate flow structure to analyze. The frequent overprediction of wind speeds has been noted in other studies such as Duine et al. (2019), which had similar RMSE values for three of their case studies and may stem from uncertainties in the land-surface parameterization and subsequent roughness length (see also De Moliner et al., 2024; Giani & Crippa, 2024). The results shown for both events exhibit both the capability of the model to resolve meso- to micro-scale flows in complex terrain and demonstrate the challenges and limitations of WRF modeling and its capacity to properly simulate such flows. However, as will be discussed in the next section, the simulations do produce realistic meso-to micro-scale flows and stability profiles that are typically associated with Sundowners especially at higher resolution.

For both events, timeseries of observed winds versus simulated winds from the d04 domain are shown at three different ISFS towers to demonstrate model forecasting skill at different geographical locations (see Figure S2 in Supporting Information S1) in order to assess model capability of capturing the complex ABL flows over complex terrain at both the SYM crest and along the adjacent southern slopes/nearby coastal regions (Figures 2a–2f). In general, the simulated output matches well with the observations in both events with MB of −3.478 to 1.695 m s^{-1} and RMSE of 2.783–5.085 m s^{-1} with the exception of ISFS tower 8 for IOP 8 (Figure 2d) where winds were underforecasted with a MB of −6.737 m s^{-1} and RMSE of 7.947 m s^{-1}. For both events, the observations, especially at the SYM crest, show a 10–15 m s^{-1} increase in wind speed just after sunset during IOP 1 (maximum observed winds of 13–24 m s^{-1}) or just before sunset for IOP 8 (maximum wind speeds of 13–25 m s^{-1}). For IOP 8, the strong winds prior to sunset are due to strong synoptic forcing which caused winds to increase in magnitude during the late afternoon of 8 May 2022. Examining the time series of observed winds and simulated winds for the d01–d03 domains indicates that increasing the model grid spacing only marginally impacts the statistical metrics of flow accuracy for point predictions with the exception of d01 domain output versus ISFS tower 11 in IOP 1 (Figures S3 and S4 in Supporting Information S1).

3.2. Simulation of Sundowners Across d01–d04 WRF Model Resolutions

In this section, we describe the results of the simulations of both Sundowner events across the domains d01–d04, at the time when Sundowner winds were strong with a clear downslope flow regime over the southern SYM slopes, in order to elucidate the importance of high-resolution modeling coupled with high-resolution topography data. We evaluate the stability and mountain wave pattern along north to south cross sections drawn through the d04 domains (see Figures 1b and 1e) and the total horizontal 10 m flow (10 m winds hereafter) across the SYM region and adjacent coastal regions. The d05 domains are omitted from analysis in this section because of their relatively small size making comparisons with the other domains not possible over most of the SYM region.

The cross-sectional analyses of the Sundowner events in terms of stability, mountain-waves and cross-mountain flow are performed along regions of maximum flow, which cross areas upstream of the SYM, the SYM, the adjacent coastal regions, and extend over the Pacific. The importance of topography data together with higher resolution modeling is evident in Figure 3. For both IOPs, in both the d01 and d02 domains, the SYM are smoothed to just a gentle rising slope owing to the standard GMTED topography data (resolution of 900 m) being upscaled into the mesoscale domains. Despite this gentle rising slope, the simulated meridional flow parallel to the cross-section (v_{cross} hereafter) still indicates stronger low-level flow in the vicinity of the SYM beneath and within a stable layer, shown by a vertical gradient of potential temperature (Θ), $d\Theta/dz = 1$ K 100 m^{-1}. Very little, if any, mountain wave activity appears in the d01 and d02 domains, except for the d02 domain where hints of mountain waves are seen in the isentropes which fold downward on the south side of the SYM (Figure 3f). The mountain wave pattern and subsequent downslope flow are much more apparent in the d03 and d04 resolutions (Figures 3c, 3d, 3g, and 3h) where the SYM mountains are distinct and a stable layer atop the crest of the mountains folds downward along the southern slopes with stronger v_{cross} of 20–25 m s^{-1} and locally higher in the IOP 8 event (Figure 3d). An analysis of the F_r number indicates a transition from $F_r > 1$ to <1 over the southern SYM slopes signifying a transition from supercritical to subcritical flow, a hydraulic jump signature for domains d01–d04 in IOP 1. For IOP 8, the hydraulic jump signature only appears in the d03 and d04 domains whereas strong synoptic flow allows for strong near-surface flow in d01 and d02 domain despite no hydraulic jump signature (Figures 3a and 3b).

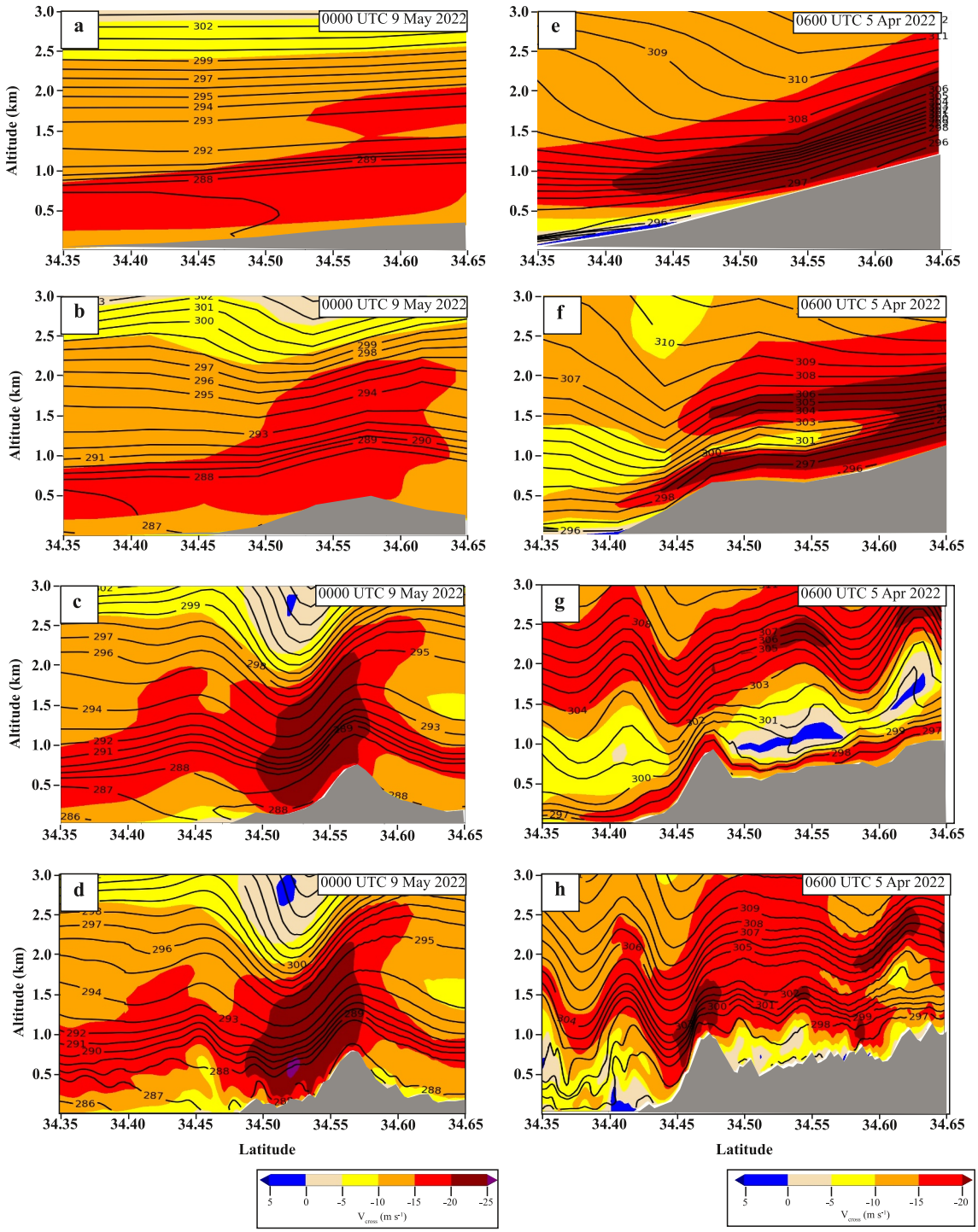

Figure 3. WRF simulated v_{cross} (m s^{-1}, color shading) and Θ (K, isentropes) for (a) d01; (b) d02; (c) d03; (d) d04 for 0000 UTC 9 May 2022 (IOP 8); and (e) d01; (f) d02; (g) d03; (h) d04 for 0600 UTC 5 April 2022 (IOP 1).

The spatiotemporal variability of both events is shown in simulated 10 m winds. The western event, IOP 8, exhibits significant differences in the simulated 10 m winds between the lower resolution domains (d01–d02) and the higher resolution domains (d03–d04) at 0000 UTC 9 May 2022 (Figure S5 in Supporting Information S1). The regions "A," "B," and "C" in Figure S5 of the Supporting Information S1 highlight important features tied to the complex terrain in the d04 domains for each event that are not found at such detail at lower resolutions. In Figures

S5a and S5b of the Supporting Information S1 a broad, fairly uniform northwesterly flow is found across the western SYM with 10 m winds of 10–17.5 m s^{-1} over much of the domain. The impact of the 30 m SRTM topography data is evident with a clear increase of northerly 10 m winds to 20–25 m s^{-1} on the southern slopes of the SYM (Figures S5c and S5d in Supporting Information S1). A weaker westerly flow of 5–10 m s^{-1} with locally higher values is found near the coast. Offshore, 10 m winds are again northwesterly and increased in speed to 12.5 to, in some areas, ∼20 m s^{-1} (Figure S5c in Supporting Information S1). In Figure S5d of the Supporting Information S1, the northerly downslope flow exceeds 25 m s^{-1} ("A") in some pockets on the southern SYM slopes. Compared to Figure S5c in Supporting Information S1, the northerly flow has greater spatial variability on the southern SYM tied to the complex SYM topography. Again, a weaker westerly flow is in the coastal regions ("B") whereas a stronger northwesterly flow of 10–20 m s^{-1} is shown offshore including channels of stronger 17.5–20 m s^{-1} flow in northwest to southeast oriented lines ("C").

For IOP 1, at the coarsest resolution, north to northeast 10 m winds of 10–14 m s^{-1} are found at the northeast corner of the region with a westerly flow of 2–6 m s^{-1} by the coast (Figure S5e in Supporting Information S1). In the d02 domain, a stronger northerly flow of 8–12 m s^{-1} is found over the eastern SYM, which increases to 12–16 m s^{-1} extending from the eastern SYM region southward to over the Pacific in the d03 domain (Figures S5f and S5g in Supporting Information S1). The 10 m winds in the d04 domain have two maxima located near the crest and immediate southern slopes ("A") of the SYM with northerly 10 m winds of 16–20 m s^{-1} with locally higher values (Figure S5h in Supporting Information S1). In the coastal region, a weak westerly flow of around 5 m s^{-1} is found ("B") with a stronger northwesterly flow further offshore ("C").

Since the combination of high-resolution topography data and simulated flows in the d04 domain are most realistic and captured the downslope flows and mountain wave patterns, these will be used in the next section to give more detailed analyses of both Sundowner events.

3.3. Analysis of Meso- to Micro-Scale Features and Drivers

An analysis of both simulated Sundowner events during peak intensity is presented in this section using output from the d04 domains. We first present an analysis of 10 m winds, mean sea-level pressure (MSLP), 2 m temperature (T), for each event followed by cross-sectional analyses of v_{cross} and stability to characterize the Sundowners.

Each event featured a strong northerly downsloping flow on the crest of and along the southern SYM slopes, weak westerly flow along the coastal regions, and stronger north or northwesterly flow offshore over the Pacific. Three regions of interest are labeled ("A"), ("B"), and ("C") in both Figures 4 and 5. For the IOP 1, Region ("A") notes a west-northwest-east-southeast aligned region of northerly 10 m winds of 15–20 m s^{-1} and in some pockets, >20 m s^{-1} (Figures 4a–4d). This region is collocated with the crest of the SYM mountain and the southern slopes where winds remained strong throughout the peak intensity of the event. Just south of this region of winds, ("B") highlights weaker westerly 10 m winds of 3–6 m s^{-1} that are consistently found along the coastal region, which is relatively unaffected by the Sundowner and are consistent with local observations in Montecito, CA (not shown). The other regions of interest are noted by ("C"), which denotes regions of northerly to northwesterly offshore flow of 12–16 m s^{-1} and locally as high as 18 m s^{-1}. These two local maxima are located between 1 and 2 km off the coast and since they both area regions of the same flow regime, ("C") will be used for both maxima when they are present.

The IOP 8 Sundowner featured a strong northwesterly flow that was present in the afternoon of 8 May 2022 and continued into the overnight period of 9 May 2022. The simulated 10 m winds for this case show a strong northwesterly flow across much of the region shown at 0000 UTC 9 May 2022, roughly 3 hr before sunset (Figure 5a). Nevertheless, downsloping 10 m winds of 15–25 m s^{-1}, and locally higher in some spots, are simulated along the southern slopes of the SYM at ("A") between 0000 and 0600 UTC May 2022 with only slight weakening afterward (Figures 5a–5d). Similar to IOP 1, a weaker westerly flow of ∼5 m s^{-1} is located along the coastal region south of the SYM slopes at ("B") and a stronger 10–20 m s^{-1} northwesterly flow is found offshore at locations marked by ("C") (Figures 5a and 5b). The weak westerly coastal flow continues at ("B") until 0900 UTC when a slight veering to northwest occurs (Figures 5b–5d). Meanwhile, the northwesterly offshore flow continues near places labeled ("C") with a slow diminishing trend with 10 m winds of 10–15 m s^{-1} by 0900 UTC (Figures 5b–5d).

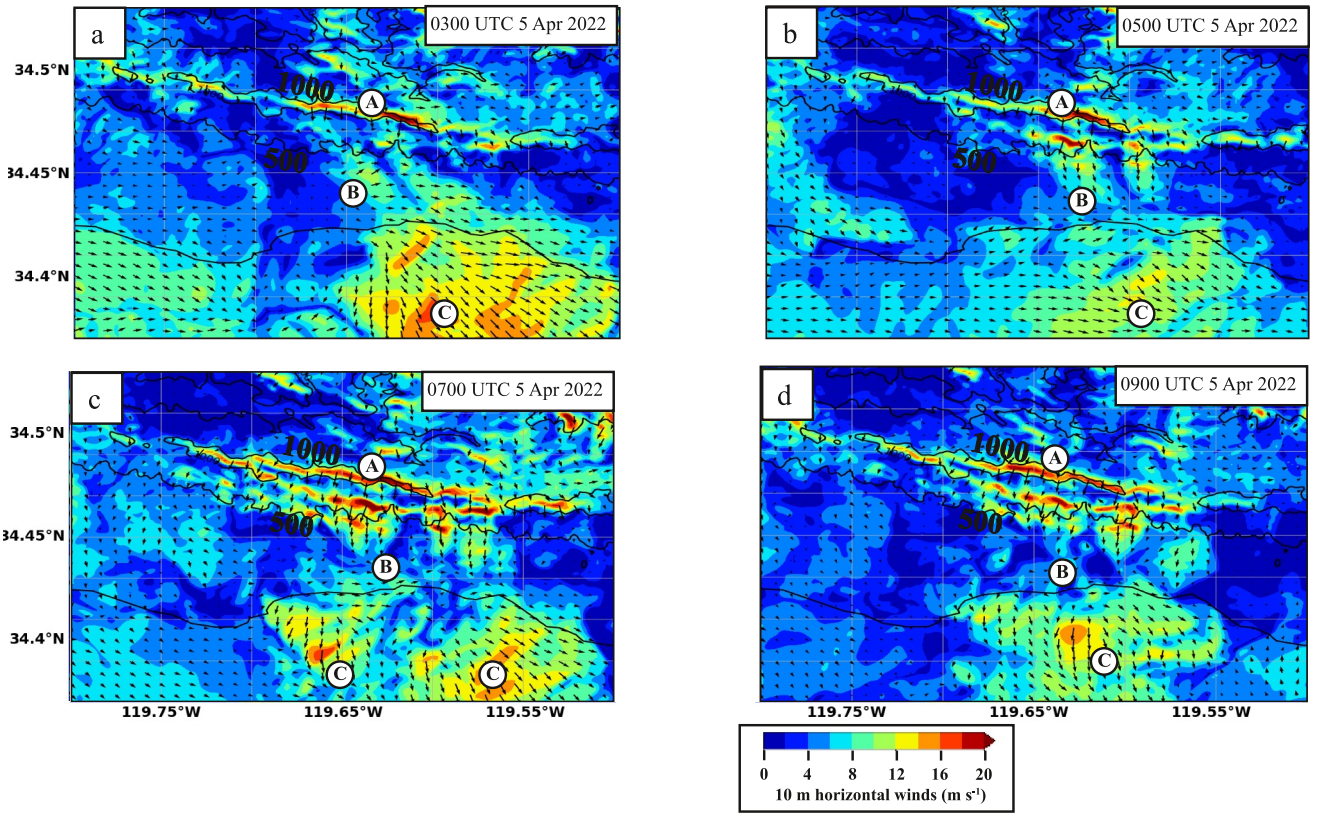

Figure 4. WRF simulated 10 m winds (m s^{-1}) at 2-hr intervals from 0300 UTC to 0900 UTC on 5 April 2022 (IOP 1) over the d04 domain. Areas of interest to be discussed in the text are labeled "A," "B," and "C." Terrain contours (m) and labels are in black.

Analyzing simulated MSLP and *T* for each event shows the meso- to -micro-scale changes of each throughout the duration of both events. During IOP 8 peak wind intensity times, local minima in MSLP are simulated along the southern slopes of the SYM, collocated with the strongest downslope flows, with MSLP of 1,004–1,008 hPa. Higher MSLP of 1,014–1,016 hPa is found to the north of the SYM with lower values of 1,012–1,014 hPa immediately south of the SYM (Figures 6b and 6c). The *T* fields show evidence of adiabatic warming as a result of the downslope flow regime (Figures 6d–6f). Local *T* maxima are found along and just south of the southern SYM slopes in all three panels and also coincided with a decrease of specific humidity (not shown). Despite cooling after sunset, which was at 0250 UTC (note difference in *T* between Figures 6d and 6e), *T* was 2–6 K warmer along the region immediately adjacent to the southern SYM slopes when compared to other nearby coastal regions on the east side of the region shown (Figures 6e and 6f). During the 0300–0900 UTC, areas outside the warmer region due to the adiabatic warming continued to cool by ∼1K hr^{-1} (not shown), whereas the warmer region on the southern slopes maintained a steady temperature of 284–286 K. Again, the coolest *T* is found atop the SYM with *T* of 282–286 K after sunset. Slightly warmer *T* of ∼2 K is found over the Pacific directly south of the location of the strongest downslope winds compared to other locations nearby.

At the start of the IOP 1 event, little MSLP differences exist over the eastern SYM range with a few pockets of 1,014–1,016 hPa found on the northern side of the SYM with 1,010–1,012 hPa found along the coast and over the Pacific (Figure 6g). All other areas had MSLP between 1,012 and 1,014 hPa. At 0600 UTC and afterward, MSLP increases on the north side of the SYM to 1,014–1,016 hPa with a few pockets of 1,010–1,012 hPa along the crest and slopes of the SYM (Figures 6h and 6i). This results in an increased pressure gradient across the SYM and is coincident with the increase in magnitude of the Sundowner winds seen in Figures 4b–4d. The increase of MSLP to the north of the SYM and subsequent stronger pressure gradient between the SB region and the northern side of the SYM have been documented in previous research as an important causal factor in Sundowner events (Blier, 1998; Ryan, 1996).

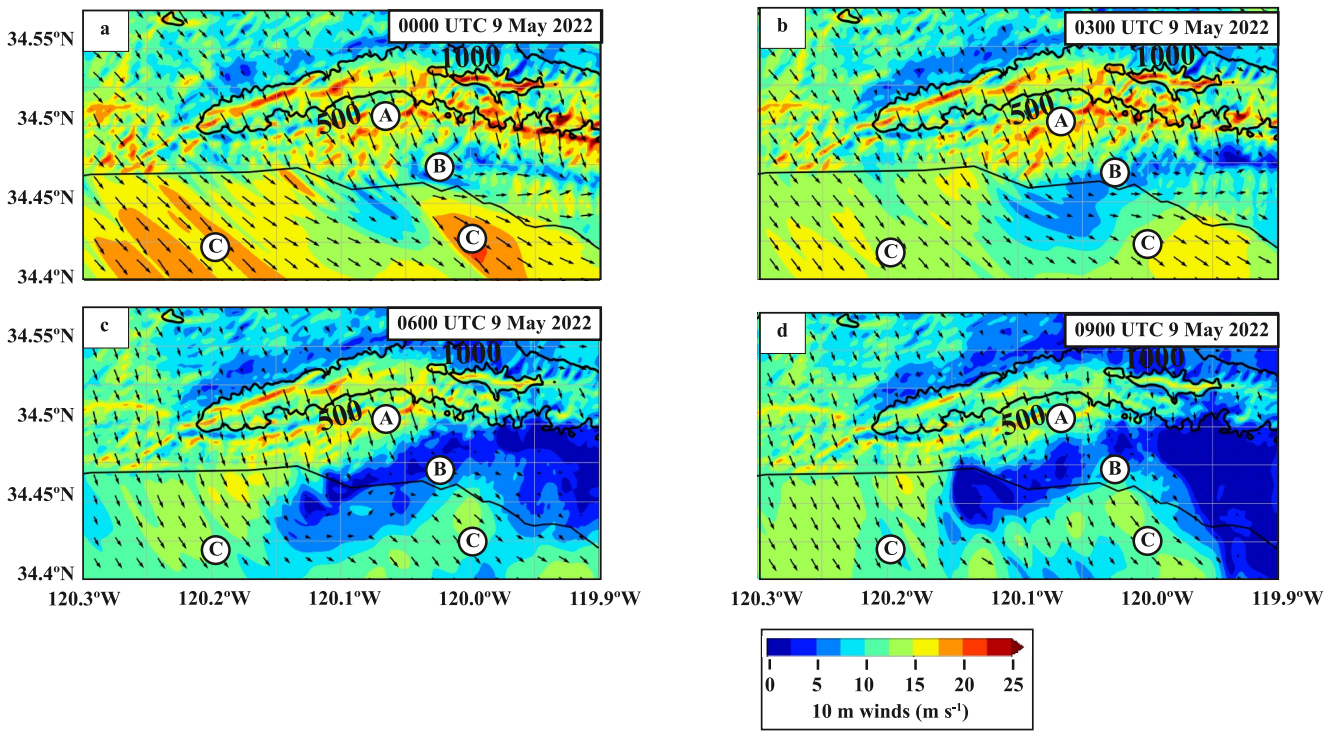

Figure 5. WRF simulated 10 m winds (m s^{-1}) at 3-hr intervals from 0000 UTC to 0900 UTC 9 May 2022 (IOP 8) over the d04 domain. Areas of interest to be discussed in the text are labeled "A," "B," and "C." Terrain contours (m) and labels are in black.

The simulated T fields show pockets of T = 294–298 K located on the southern slopes of the SYM near the location of the strongest flow (see arrows in Figures 4c and 4d) while the coolest T of 282–284 K are found at the crest of the SYM (Figures 6k and 6l). Outside of the warm "pockets" temperatures continued to cool by 1–3 K between 0300 and 0900 UTC indicating the warm "pockets" are due to adiabatic warming of descending air off the SYM. This temperature distribution, and also a slight drying of the near-surface air at the base of the SYM (not shown), is indicative of adiabatic warming and drying due to downsloping winds. Meanwhile, warmer T = 294–298 K remained offshore over much of the Pacific directly to the south of the Sundowner region (Figures 6k and 6l).

3.4. Cross Section Analysis of Winds and Stability

3.4.1. Analysis of Mountain Wave Activity and Meridional Flow Behavior

A cross-sectional analysis using d04 resolution output is performed to characterize the simulated Sundowner events in terms of mountain waves, atmospheric stability, marine boundary layer (MBL) interactions and quantify the magnitudes of both horizontal and vertical winds. Both Sundowner events are characterized by a clear mountain wave pattern with downsloping flows on the south side of the SYM. The warming and drying of the downslope flows likely resulted in a deepening adiabatic layer near coastal regions with the downslope flows ascending over the coastal regions then descending to the surface offshore over the Pacific.

Previous work has highlighted the MBL as a factor in Sundowner events and in order to diagnose its role in each event, analyses are conducted prior to the time of peak intensity to show the interaction and evolution of v_{cross} with the MBL. The MBL is more prevalent in the IOP 1 especially toward the end of the event while in IOP 8 there is no MBL influence. Figure 7a, in particular, shows the presence of a stable MBL over the Pacific Ocean in the lowest 250 m of the atmosphere denoted by a vertical Θ gradient ($d\Theta/dz$) of ~1 K 100 m^{-1} at 0400 UTC 5 April (Figure 7a). This stable layer erodes quickly by 0600 UTC, and there is no evidence that the MBL was a major factor in the event.

The cross-sectional analysis of the IOP 1 Sundowner event elucidates many multiscale features of this event. Mountaintop stability increases after 0400 UTC 5 April 2022 to 1 K 100 m^{-1} at "A" between the SYM crest and

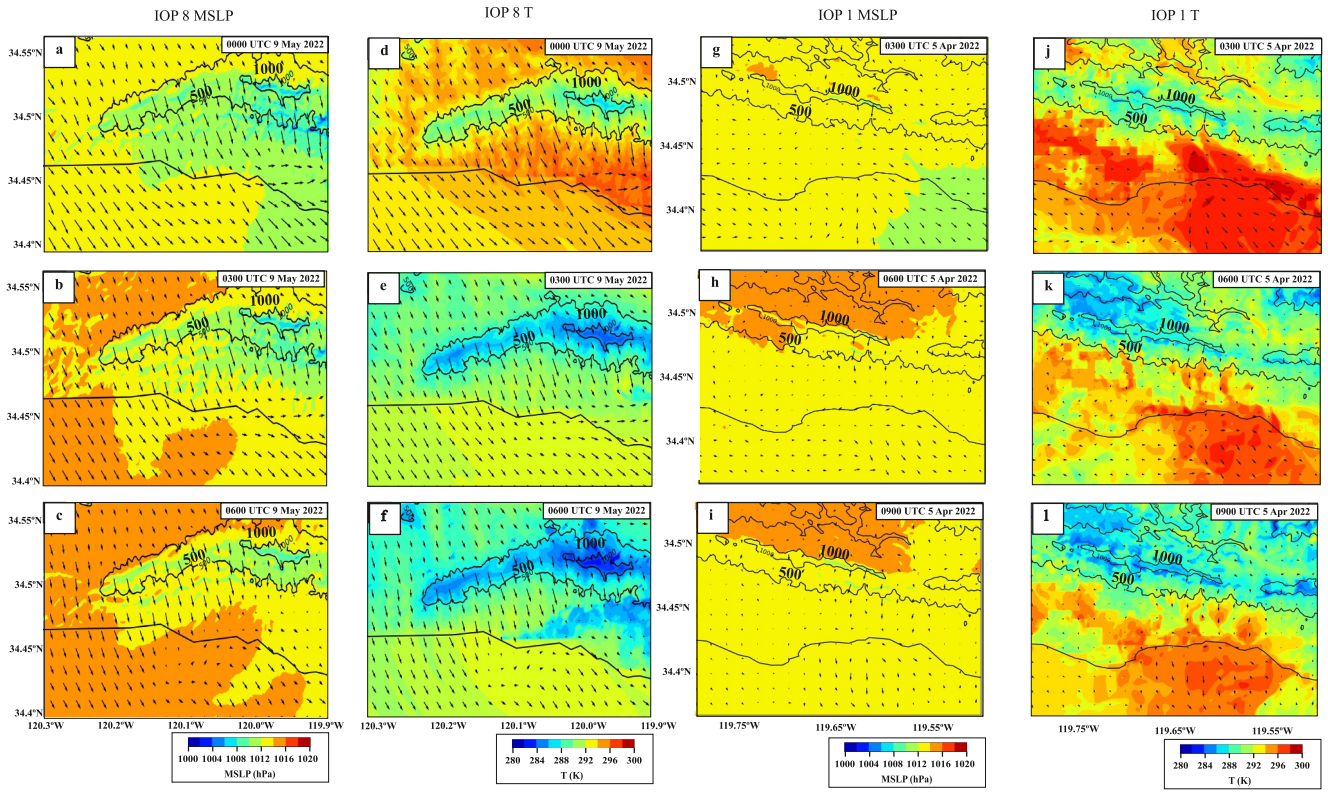

Figure 6. WRF simulated MSLP (shaded, hPa), (columns 1 and 3) and T (K, columns 2 and 4) both overlaid with 10 m wind vectors. Different rows display model output every 3 hr for each variable. All times (in UTC) in (a)–(f) are for 9 May 2022 (IOP 8), whereas times in (g)–(l) are for 5 April 2022 (IOP 1). Terrain contours (m) and labels are in black.

1.5 km altitude coinciding with a downward folding of the stable layer over the southern SYM slopes with the region of tightly packed isentropes extending down from its crest atop the SYM crest at ~1 km altitude to ~0.5 km altitude between "A" and "B," consistent with mountain lee waves (Grubišić & Billings, 2008). In the same region, magnitudes of v_{cross} increase to—15 to −20 m s^{-1}, with locally higher magnitudes, atop the SYM crest along the southern SYM slopes between 0600 and 0800 UTC (Figures 7a–7c). Downstream of the strong downslope flow, an adiabatic layer with $d\Theta/dz = 0$ between the surface and ~0.7 km altitude is found near "B" from 0600 to 0800 UTC (Figures 7b and 7c). This layer is likely a result from the adiabatic warming of the downslope flow descending the southern SYM slopes (see Figures 6j–6l). Also near "B," the strong downslope winds are seen to be channeled atop the adiabatic layer with v_{cross} of −15 to −20 m s^{-1} between 0.5 and 1.5 km altitude during the 0600–0800 UTC timeframe with much weaker flow beneath. During the same timeframe, v_{cross} reverses direction near "B" between the surface and ~250 m altitude with values of up to 5 m s^{-1} (Figures 7b and 7c). As will be discussed more later, the low-level reversal of v_{cross} suggests the possibility of a rotor, which can occur in such downslope flow regimes (Grubišić & Billings, 2008). Further downstream, over the Pacific, a belt of stronger v_{cross} of −10 to −15 m s^{-1} at 0600 UTC, strengthening to −15 to −20 m s^{-1} at 0800 UTC, is shown reaching the surface by "C" (Figures 7b and 7c). As shown earlier, 10 m horizontal winds increased offshore supporting the v_{cross} pattern.

In order to more quantitatively describe the mountain wave pattern, overlays of WRF simulated vertical velocity (w, hereafter) (m s^{-1}) with R_i are shown along the cross section (Figures 7e–7h). Throughout the Sundowner event, $R_i < 0.25$ was simulated within 100–500 m of the surface over land signifying a critical layer. In particular, between 0600 and 1000 UTC, $R_i < 0.25$ is collocated with a −4 to −5 m s^{-1} downdraft over the southern SYM slope (Figures 7f–7h). Further evidence supporting mountain waves is shown in the F_r overlays between 0600 and 1000 UTC (Figures 7j–7l). A hydraulic jump signature is highlighted by the transition of $F_r > 1$ to $F_r < 1$ at the southern base of the SYM indicating a transition from supercritical to subcritical flow. These findings lead to the conclusion that during the peak of this event, the strong downslope flow is a result of a mountain waves over the

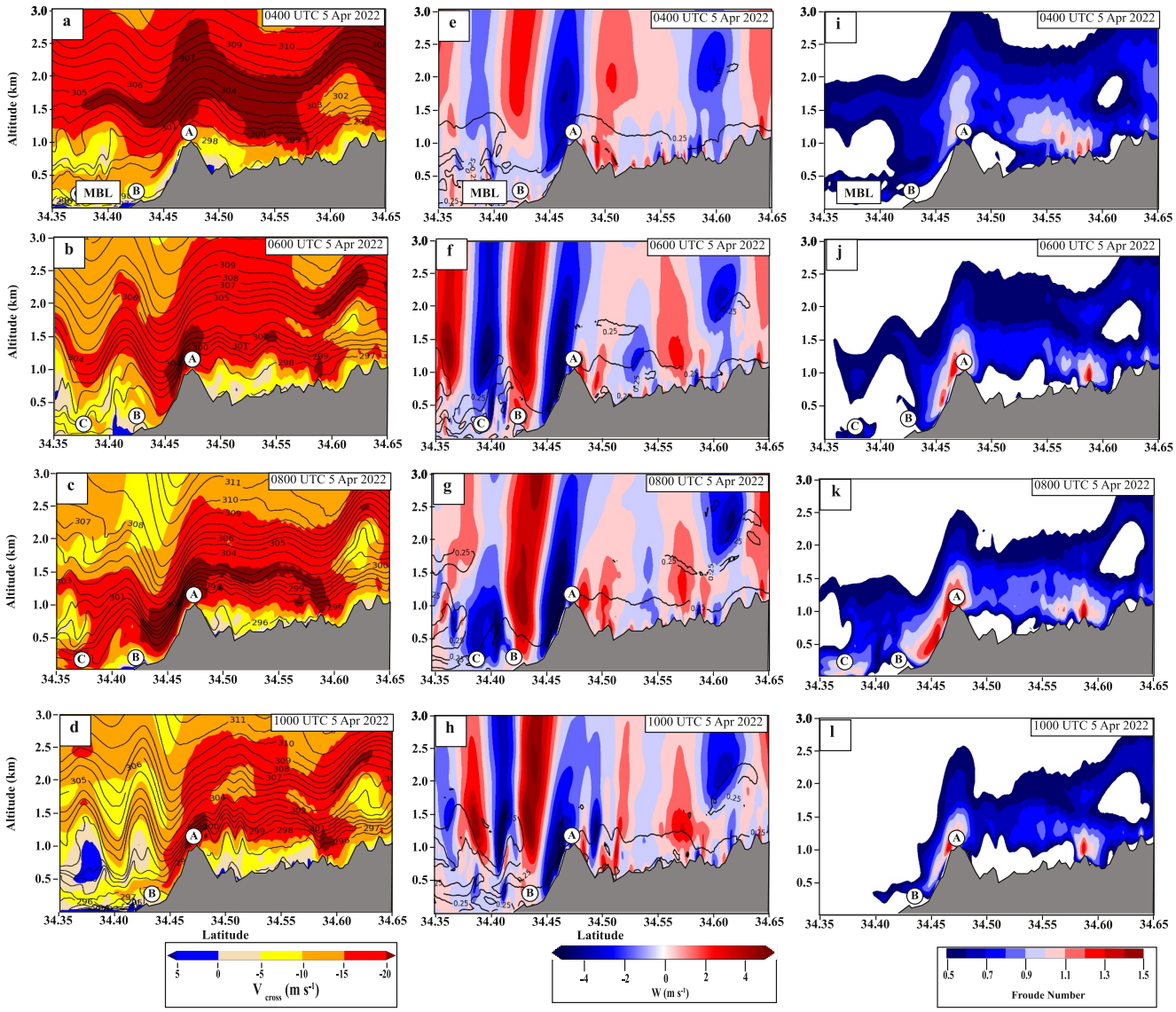

Figure 7. (a–d) WRF simulated v_{cross} (m s^{-1}) and Θ (K, isentropes), (e–h) WRF w (m s^{-1}) and $R_i = 0.25$ contour, and (i–l) WRF F_r for 2-hr intervals from 0000 to 1000 UTC 5 April 2022 (IOP 1). Areas of interest to be discussed in the text are "A," "B," "C," and "MBL."

SYM crest and lee slopes characterized by an increase of v_{cross} magnitudes coincident with increased mountaintop stability, a stable layer folding downward along the southern SYM slopes, near surface $R_i < 0.25$ critical layer collocated with a downdraft of −4 to −5 m s^{-1}, and a transition from supercritical to subcritical flow signified by the F_r.

The IOP 1 Sundowner diminished around and after 1000 UTC 5 April 2022 as shown by the decrease in v_{cross} both upstream of the SYM and over the Pacific and mountaintop stability slowly decreasing with time (Figure 7d). As the event diminished, multiple waves between 0.5 and 1.5 km altitude over the Pacific with another region of reversed v_{cross} of 0–5 m s^{-1} between 0.5 and 1 km altitude indicating another rotor signature. Increasing stability of 1 K 100 m^{-1} below 0.5 km over the Pacific likely indicates a shallow MBL that prevented the stronger v_{cross} from reaching the surface at that location.

Similar patterns are found in the cross-sectional analysis of the IOP 8 Sundowner. The acceleration of v_{cross} due to increasing stability atop the SYM is clearly depicted as the maximum v_{cross} of −20 to −25 m s^{-1}, with locally higher values, is located within a stable layer of $d\Theta/dz$ = ∼1.2 K 100 m^{-1} that exhibit a classic mountain wave signature (Carvalho et al., 2020, 2024; Grubišić & Billings, 2008), which sloped from the crest of the SYM

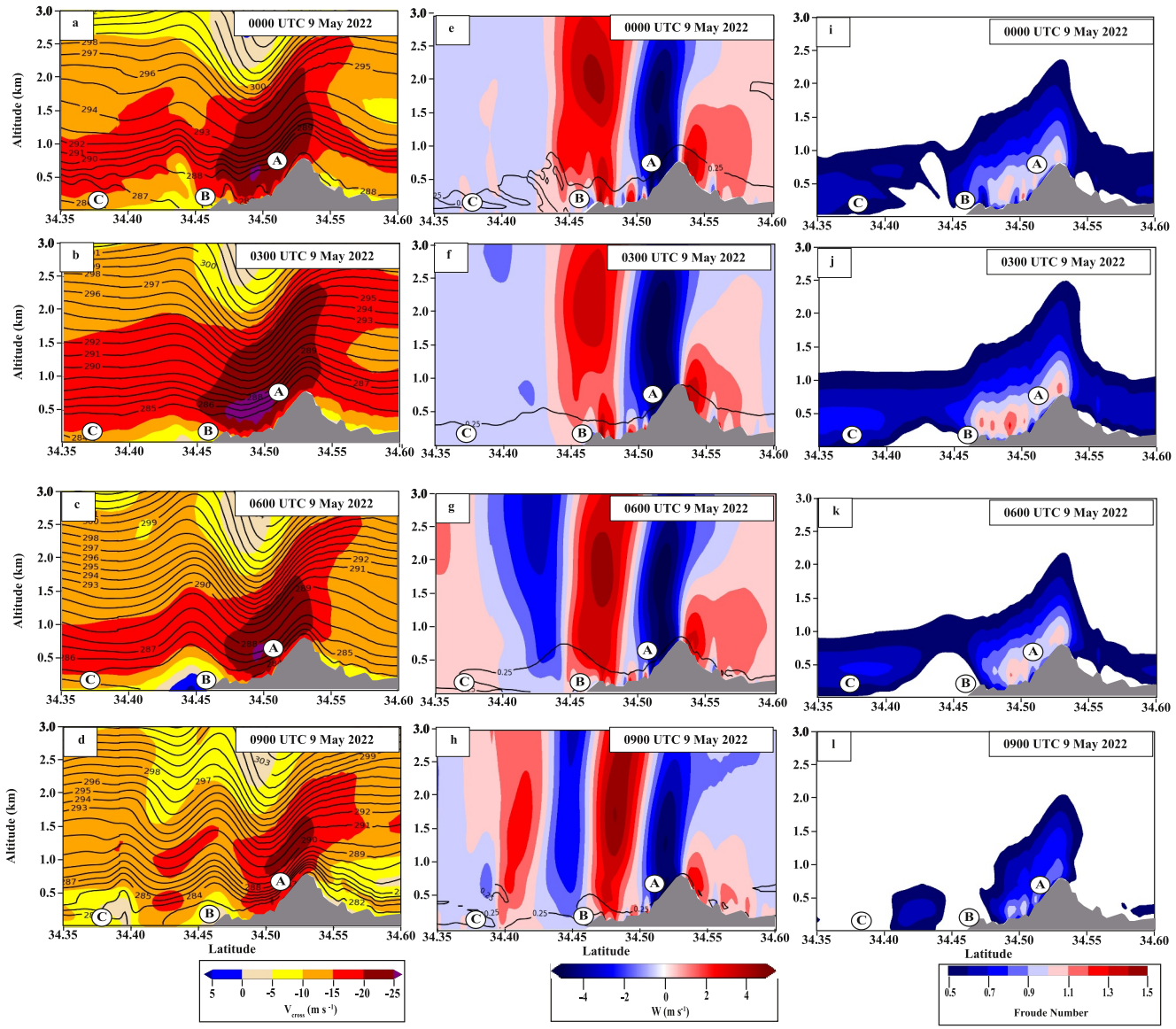

Figure 8. (a–d) WRF simulated v_{cross} (m s^{-1}) and Θ (K, isentropes), (e–h) WRF w (m s^{-1}) and $R_i = 0.25$ contour, and (i–l) WRF F_r for 2-hr intervals from 0000 to 1000 UTC 5 April 2022 (IOP 8). Areas of interest to be discussed in the text are "A," "B," "C."

downward along its southern slopes around ("A") (Figure 8). Region ("B") is the location of the weaker, or in some cases, reversal of v_{cross} with magnitudes of 0–5 m s^{-1} collocated with the weaker westerly flow shown along the coastal region in Figure 5. As with the previous case, the low-level weakening and even reversal of v_{cross} around "B" suggest the presence of a rotor. Around and after 0300 UTC, an adiabatic layer with increasing depth to 0.5 km deep is shown and likely a result of the warming and drying effect of the downsloping flow. The increase of v_{cross} to −10 to −15 m s^{-1} at the Pacific Ocean surface is highlighted by ("C") is tied to the stronger winds descending from atop the adiabatic layer at "B" to the surface and matches well with the increase northwesterly offshore flow shown in Figures 5a–5d.

Similar to the previous IOP, the WRF overlay of w and R_i show $R_i < 0.25$ within the lowest 100–500 m of the atmosphere over land and collocated with a downdraft of −4 to −5 m s^{-1} over the southern slope of the SYM throughout the event (Figures 8e–8h). Meanwhile, F_r shows a transition between supercritical and subcritical flow over the coastal region in between "A" and "B" at all times except 0900 UTC signifying another hydraulic jump (Figures 8i–8k).

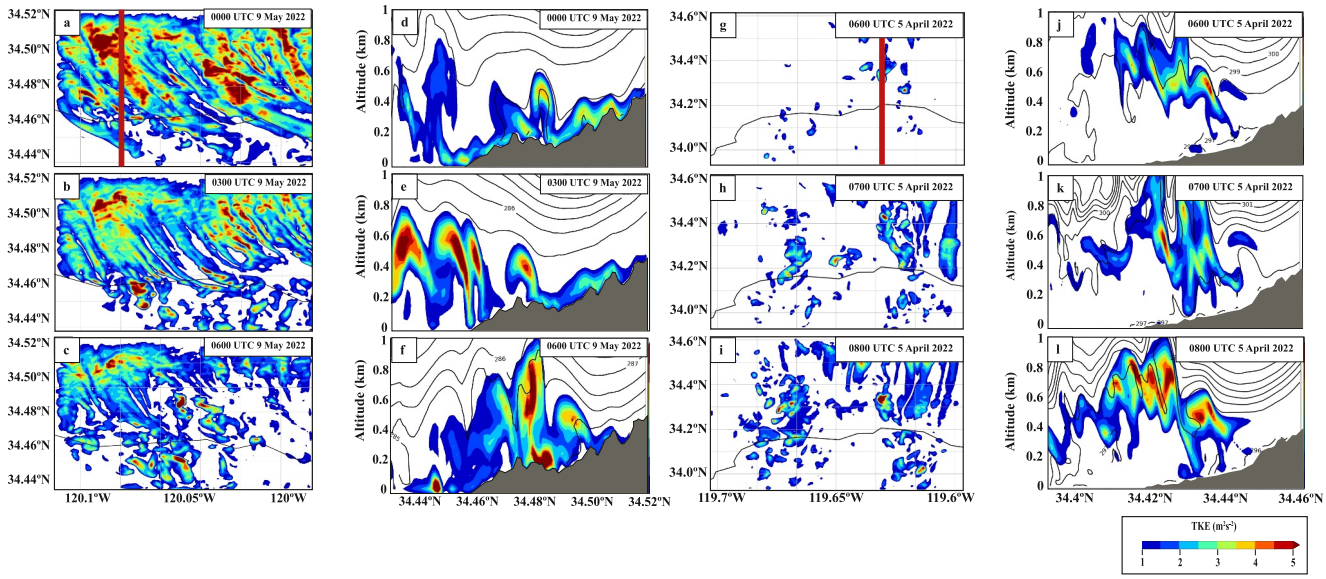

Figure 9. WRF modeled TKE ($m^2\ s^{-2}$, columns 1 and 3) and cross-sectional analysis (columns 2 and 4) with Θ (K, isentropes). Different rows display hourly output (times in UTC). All times in (a)–(f) are for 9 May 2022 (IOP 8), whereas times in (g)–(l) are for 5 April 2022 (IOP 1).

This event diminished around 0900 UTC and after as, similar to IOP 1, v_{cross} both upstream and over the SYM crest weakened along with mountain stability slowly decreasing with time (Figure 8d). These findings lead to the conclusion that during the peak of this event, the strong downslope flow is linked with increased stability at the SYM crestand along the southern SYM slopes, a stable layer folding downward with near surface $R_i < 0.25$ critical layer, a downdraft of −4 to −5 m s^{-1}, and a transition from supercritical to subcritical flow illustrated by the F_r.

3.5. Simulated TKE and ABL Evolution Over Coastal Region in d05 Domains

This section investigates the ABL behavior and the spatiotemporal distribution of simulated TKE within the inner-most d05 domains for each Sundowner event where downsloping flows interacted with adiabatic layers that exhibited turbulence.

The impact of local topography and its influence on the generation of turbulence is illustrated well during maximum Sundowner intensity in IOP 8 (Figures 9a–9f). Over the southern SYM slopes, several northwest–southeast channels of maxima in TKE of 3–5 $m^2\ s^{-2,}$ and in some cases higher are found along the southern SYM slopes and extending in some locations to just off the Pacific Coast (Figures 9a and 9b). These channels, which demonstrate the complex microscale structure of these Sundowner events, are on the order of 500 m–1.5 km wide in most locations and don't begin to weaken by 0600 UTC 9 May 2022 and afterward as shown in Figure 9c.

A north-south cross section, shown by the red line in Figure 9a, shows an adiabatic layer of 0.6–0.8 km deep, similar to Figures 8b and 8c, located near the coastline. Plumes of TKE greater than 5 $m^2\ s^{-2}$ extend from the surface to, at times, nearly 1 km altitude. Within the adiabatic layer, the low-level winds are weak westerly or west-southwesterly with the much stronger northerly downslope flow ascending over the top of the adiabatic layer (see region ("B") in Figures 8b and 8c).

Horizontal hourly distributions of TKE for IOP 1 show that turbulence is collocated with regions of stronger 10 m winds (see Figure 4c) with values, in pockets, of 3–5 $m^2\ s^{-2}$ focused in two regions of the domain. One, over a narrow corridor in the west-central part and the other over the eastern third largely over land. Even within these two regions, TKE values vary over distance and time (see differences in eastern third of domain in Figures 9g–9i). A cross section, shown by the red line in Figure 9g, is used to analyze the vertical distribution of TKE and characterize the adiabatic layer that is present. Atop this layer, turbulent wave structures are present with pockets of TKE of 3–5 $m^2\ s^{-2}$ with locally higher amounts between 0.4 and 0.8 km, which coincide with the location of

stronger northerly downslope flow being lofted over the layer while within this adiabatic layer and beneath the turbulent wave structures, a weak westerly to west-southwesterly flow is found (see region ("B") in Figures 7d and 7e).

In both IOPs, the presence of turbulence within and atop the adiabatic layer collocated with updrafts associated with the mountain wave activity (see Figures 7e–7h and 8e–8h) is a signal for a rotor as discussed in Grubišić and Billings (2008). The turbulence production is attributable to large vertical wind shear present between the strong v_{cross} within or near the stable layer atop the adiabatic layer and weaker v_{cross} beneath (see Figures 7b, 7c, 8b, and 8c).

Although the simulation of turbulence indicated that these flows are highly turbulent, and turbulence is generated within and atop adiabatic layers near the coastal regions on the lee side of the SYM, the specific impact of turbulence on the flows are beyond the scope of this study. Another complicating factor is the lack of observations of turbulence given such a complex microscale flow pattern in complex terrain. Although the ISFS towers make measurements of some of the components of turbulence, the still fairly sparse coverage of these towers on the SYM and adjacent areas makes testing model TKE output accuracy difficult.

4. Discussion and Conclusions

Although previous studies have investigated Sundowners using mesoscale grid spacing, no prior studies have used a meso-to micro-scale grid coupling, at up to 30 m grid spacing coupled with high resolution topography data, to characterize the microscale structure of such flows in the ABL. The simulations presented in this study show that the main drivers for both events are both increasing mountaintop stability and the mountain wave patterns with a hydraulic jump and near-surface critical layer. Both simulations characterized the ABL flows as having large spatiotemporal variability tied to the complex terrain of the SYM and adjacent areas and highlighted the importance of incorporating high resolution topography data to simulate such flows. Also, model predictability of such wind speeds with the Sundowners increased, generally, at higher model resolution in most locations when compared to ISFS tower observations.

Another important finding of this paper is the presence of a hydraulic jump signature over the southern SYM slopes, followed by the ascent of the downslope flows over the turbulent adiabatic layers at the coastal regions captured by WRF at high resolution. In both cases, the strong downslope flow warms and dries the air descending the southern slopes of the SYM adiabatically generating a deepening adiabatic layer that is 0.4 to as much as 1 km deep during peak Sundowner intensity over the coastal regions. This layer, exhibiting turbulence within and atop, is characterized with the strong downslope flow atop with much weaker, and at times, reversed flow beneath over the coastal regions. This flow structure, along with regions of turbulence within and atop the adiabatic layer, is indicative of a mountain lee-wave rotor associated with such flows and compares well with those studied in the Sierra Rotors Project (Grubišić & Billings, 2008). This ascent of the downslope flow over the coastal regions is not found among the majority of sensitivity simulations performed in previous research such as Carvalho et al. (2024). Further investigations are needed to determine whether or not, this is consistent across all Sundowner events observed during the SWEX project.

For both events, any MBLs are eroded away by the time of peak Sundowner intensity, consistent with the findings of observational studies such as Blier (1998), and this suggested that the MBL did not play a factor in the intensification of either IOPs 1 and 8. Only in IOP 1 is the MBL present at both the beginning and end of the event although there is no evidence that it is a major factor in the event.

Examining TKE in d05 in the regions of the adiabatic layers shows TKE is often found atop and at times, especially in IOP 8, extending throughout the 0.4–0.8 km deep layers. Also, in IOP 8, TKE is also very prevalent over the SYM crest and along the southern slopes of the SYM. The cause of the TKE is due to strong vertical wind shear between the strong downslope flow atop the adiabatic layer and weaker flow beneath. Determining the precise role of TKE in these events is beyond the scope of this paper. However, the simulated TKE from the innermost domain using high resolution topography data gives insight into the multiscale WRF model's capability to resolve the role of turbulence. Further investigations are needed to determine the contribution of turbulence to the Sundowner events and analyze whether TKE may contribute to diffuse or accelerate the downslope winds.

Other possible sources of uncertainty include sensitivity to: land-use categorization, roughness length, SGS model closure, and lateral boundary conditions. Previous work on multiscale WRF model sensitivity to different

model input factors found that sensitivity is greatest for terrain representation and land-use followed by then boundary conditions and gray zone treatment (De Moliner et al., 2024; Giani & Crippa, 2024; Giani et al., 2022). Based on those studies determining that the greatest sensitivity includes topography input, the incorporation of high-resolution topography data for the simulations done in this study gives confidence that the ABL flows are realistically simulated. However, it is possible that other model input factors may dominate the uncertainty for specific time periods (De Moliner et al., 2024), thus future work may be directed to further investigate model output sensitivity across a wider range of modeling choices and input.

A summary of the key findings of this paper are as follows:

(1) Increasing the model grid spacing only marginally impacts the statistical metrics of flow accuracy for point predictions. The structure of the Sundowner events is most realistically produced in the d04 domain (150 m grid spacing), which incorporates the high-resolution topography and most clearly simulated the mountain wave pattern.
(2) The main dynamic drivers of Sundowners in IOPs 1 and 8 are increased stability atop the SYM after sunset and the mountain wave patterns with a hydraulic jump and near-surface critical layer.
(3) Both events exhibit a strong downslope wind, over 20 m s^{-1}, which descends the southern slopes of the SYM until ascending over the coastal adiabatic layer of 0.4–0.8 km and then descending to the surface over the Pacific during the time of maximum intensity. In both events, the coastal regions are relatively unaffected.
(4) Both events showcase signs of a mountain lee-wave rotor with much weaker or even reversed flow at the bottom of the coastal adiabatic layer beneath stronger flow atop the layer downstream of the SYM. The reversed flow along with turbulence atop the adiabatic layer likely due to strong vertical wind shear matches the "footprint" of rotors observed in previous research projects such as the Sierra Rotors Project.
(5) The coastal adiabatic layer exhibits TKE of 3–5 m^2 s^{-2} with locally higher values throughout the depth of the layer in IOP 8 and atop the layer in IOP 1.

Data Availability Statement

The Weather Research and Forecasting model (WRF) can be downloaded from the National Center of Atmospheric Research (NCAR) website (Skamarock et al., 2021). We provide all the namelists for the simulations to replicate them and data processing code in Janiszeski (2025). NCAR ISFS data are obtained from NCAR's Earth Observing Laboratory (EOL) data archive https://doi.org/10.5065/D6ZC80XJ. ERA5 reanalysis initial and boundary conditions are obtained from the Research Data Archive at the National Center for Atmospheric Research, Computational and Information Systems Laboratory (https://rda.ucar.edu/datasets/ds633.0/). SRTM data are obtained from USGS https://doi.org/10.5066/F7F76B1X.

Acknowledgments
This study is based upon work supported by the National Science Foundation under Grant 2236504 to Paola Crippa. Partial support is for this work is provided by the Notre Dame Environmental Change Initiative to Andrew Janiszeski.

References

Beck, J., Brown, J., Dudhia, J., Gill, D., Hertneky, T., Klemp, J., et al. (2020). An evaluation of a hybrid, terrain-following vertical coordinate in the WRF-based RAP and HRRR models. *Weather and Forecasting*, *35*(3), 1081–1096. https://doi.org/10.1175/WAF-D-19-0146.1

Blier, W. (1998). The Sundowner winds of Santa Barbara, California. *Weather and Forecasting*, *13*(3), 702–716. https://doi.org/10.1175/1520-0434(1998)013<0702:TSWOSB>2.0.CO;2

Cannon, F., Carvalho, L. M. V., Jones, C., Hall, T., Gomberg, D., Dumas, J., & Jackson, M. (2017). WRF simulation of downslope wind events in coastal Santa Barbara County. *Atmospheric Research*, *191*, 57–73. https://doi.org/10.1016/j.atmosres.2017.03.010

Cao, Y., & Fovell, R. G. (2016). Downslope windstorms of San Diego County. Part I: A case study. *Monthly Weather Review*, *144*(2), 529–552. https://doi.org/10.1175/MWR-D-15-0147.1

Carvalho, L., Duine, G., Jones, C., Zigner, K., Clements, C., Kane, H., et al. (2020). The Sundowner winds experiment (SWEX) pilot study: Understanding downslope windstorms in the Santa Ynez mountains, Santa Barbara, California. *Monthly Weather Review*, *148*(4), 1519–1539. https://doi.org/10.1175/MWR-D-19-0207.1

Carvalho, L. M. V., Duine, G., Clements, C., De Wekker, S. F. J., Fernando, H. J. S., Fitzjarrald, D. R., et al. (2024). The Sundowner winds experiment (SWEX) in Santa Barbara, California: Advancing understanding and predictability of downslope windstorms in coastal environments. *Bulletin of the American Meteorological Society*, *105*(3), E532–E558. https://doi.org/10.1175/BAMS-D-22-0171.1

Daniels, M. H., Lundquist, K. A., Mirocha, J. D., Wiersema, D. J., & Chow, F. K. (2016). A new vertical grid nesting capability in the Weather Research and Forecasting (WRF) Model. *Monthly Weather Review*, *144*(10), 3725–3747. https://doi.org/10.1175/mwr-d-16-0049.1

Deardorff, J. W. (1980). Stratocumulus-capped mixed layers derived from a three-dimensional model. *Boundary-Layer Meteorology*, *18*(4), 495–527. https://doi.org/10.1007/BF00119502

De Moliner, G., Giani, P., Lonati, G., & Crippa, P. (2024). Sensitivity of multiscale large Eddy simulations for wind power calculations in complex terrain. *Applied Energy*, *364*(2024), 123195. https://doi.org/10.1016/j.apenergy.2024.123195

Duine, G.-J., Jones, C., Carvalho, L. M. V., & Fovell, R. G. (2019). Simulating Sundowner winds in coastal Santa Barbara: Model validation and sensitivity. *Atmosphere*, *10*(3), 155. https://doi.org/10.3390/atmos10030155

Durran, D. R. (1990). Mountain waves and downslope winds. In *Atmospheric processes over complex terrain*, *Meteorological Monographs* (Vol. 23, pp. 59–81). American Meteorological Society.

Durran, D. R. (2003). In G. North, J. Pyle, & F. Zhang (Eds.), *Downslope winds. Encyclopedia of atmospheric sciences* (pp. 644–650). Elsevier.
Durran, D. R., & Klemp, J. B. (1987). Another look at downslope winds. Part II: Nonlinear amplification beneath wave-overturning layers. *Journal of the Atmospheric Sciences*, *44*(22), 3402–3412. https://doi.org/10.1175/1520-0469(1987)044,3402:ALADWP.2.0.CO;2
European Centre for Medium-Range Weather Forecasts. (2019). *ERA5 reanalysis (0.25 degree latitude-longitude grid)*. Research Data Archive at the National Center for Atmospheric Research, Computational and Information Systems Laboratory. https://doi.org/10.5065/BH6N-5N20
Fovell, R., & Gallagher, A. (2018). Winds and gusts during the Thomas fire. *Fire*, *1*(3), 47. https://doi.org/10.3390/fire1030047
Gallus, W. A., Jr., & Klemp, J. B. (2000). Behavior of flow over step orography. *Monthly Weather Review*, *128*(4), 1153–1164. https://doi.org/10.1175/1520-0493(2000)128,1153:BOFOSO.2.0.CO;2
Giani, P., & Crippa, P. (2024). On the sensitivity of large-eddy simulations of the atmospheric boundary layer coupled with realistic large-scale dynamics. *Monthly Weather Review*, *152*(4), 1057–1075. https://doi.org/10.1175/MWR-D-23-0101.1
Giani, P., Genton, M. G., & Crippa, P. (2022). Modeling the convective boundary layer in the terra incognita: Evaluation of different strategies with real-case simulations. *Monthly Weather Review*, *150*(5), 981–1001. https://doi.org/10.1175/MWR-D-21-0216.1
Grubišić, V., & Billings, B. J. (2007). The intense lee-wave rotor event of Sierra Rotors IOP 8. *Journal of the Atmospheric Sciences*, *64*(12), 4178–4201. https://doi.org/10.1175/2006JAS2008.1
Grubišić, V., & Billings, B. J. (2008). Summary of the Sierra rotors project wave and rotor events. *Atmospheric Science Letters*, *9*(4), 176–181. https://doi.org/10.1002/asl.200
Hatchett, B. J., Smith, C. M., Nauslar, N. J., & Kaplan, M. L. (2018). Synoptic-scale differences between Sundowner and Santa Ana wind regimes in the Santa Ynez Mountains, California. *Natural Hazards and Earth System Sciences*, *18*(2), 419–427. https://doi.org/10.5194/nhess-18-419-2018
Haupt, S. E., Kosovic, B., Shaw, W., Berg, L. K., Churchfield, M., Cline, J., et al. (2019). On bridging a modeling scale gap: Mesoscale to microscale coupling for wind energy. *Bulletin of the American Meteorological Society*, *100*(12), 2533–2550. https://doi.org/10.1175/bams-d-18-0033.1
Hersbach, H., Bell, B., Berrisford, P., Hirahara, S., A Horányi, A., Muñoz-Sabater, J., et al. (2020). The ERA5 global reanalysis. *Quarterly Journal of the Royal Meteorological Society*, *146*(730), 1999–2049. https://doi.org/10.1002/qj.3803
Hong, S. –Y., Noh, Y., & Dudhia, J. (2006). A new vertical diffusion package with an explicit treatment of entrainment processes. *Monthly Weather Review*, *134*(9), 2318–2341. https://doi.org/10.1175/MWR3199.1PDF
Janiszeski, A. (2025). janiszeski/JGR_manuscipt:JGR-manuscript-final [WRF namelists and processing codes]. https://doi.org/10.5281/zenodo.14736178
Jiang, Q., & Doyle, J. D. (2008). Diurnal variation of downslope winds in Owens Valley during the Sierra rotor experiment. *Monthly Weather Review*, *136*(10), 3760–3780. https://doi.org/10.1175/2008MWR2469.1
Jones, C., Carvalho, L. M. V., Duine, G.-J., & Zigner, K. (2021). Climatology of Sundowner winds in coastal Santa Barbara, California, based on 30-yr high resolution WRF downscaling. *Atmospheric Research*, *249*, 105305. https://doi.org/10.1016/j.atmosres.2020.105305
Klemp, J. B., & Lilly, D. R. (1975). The dynamics of wave-induced downslope winds. *Journal of the Atmospheric Sciences*, *32*(2), 320–339. https://doi.org/10.1175/1520-0469(1975)032,0320:TDOWID.2.0.CO;2
Kolden, C., & Abatzoglou, J. (2018). Spatial distribution of wildfires ignited under katabatic versus non-katabatic winds in Mediterranean Southern California USA. *Fire*, *1*(2), 19. https://doi.org/10.3390/fire1020019
Lawson, J., & Horel, J. (2015). Analysis of the 1 December 2011 wasatch downslope windstorm. *Weather and Forecasting*, *30*, 115–135. https://doi.org/10.1175/WAF-D-13-00120.1
Lundquist, K. A., Chow, F. K., & Lundquist, J. K. (2010). An immersed boundary method for the weather research and forecasting model. *Monthly Weather Review*, *138*(3), 796–817. https://doi.org/10.1175/2009MWR2990.1
NSF NCAR—Earth Observing Laboratory. (1990). NCAR integrated surface flux system (ISFS). *NSF NCAR—Earth Observing Laboratory*. https://doi.org/10.5065/D6ZC80XJ
Ronda, R. J., Steeneveld, G. J., Heusinkveld, B. G., Attema, J. J., & Holtslag, A. A. (2017). Urban finescale forecasting reveals weather conditions with unprecedented detail. *Bulletin of the American Meteorological Society*, *98*(12), 2675–2688. https://doi.org/10.1175/BAMS-D-16-0297.1
Ryan, G. (1996). Downslope winds of Santa Barbara, California. NOAA Technical Memorandum NWS WR 240. 44. https://repository.library.noaa.gov/view/noaa/14746
Skamarock, W. C., Klemp, J. B., Dudhia, J., Gill, D. O., Liu, Z., Berner, J., et al. (2021). A description of the advanced research WRF model version 4.3 (No. NCAR/TN-556+STR). https://doi.org/10.5065/1dfh-6p97
Smith, C., Hatchett, B., & Kaplan, M. (2018). Characteristics of Sundowner winds near Santa Barbara, CA, from a dynamically downscaled climatology: Environment and effects aloft and offshore. *Journal of Geophysical Research: Atmospheres*, *123*(23), 13092–13110. https://doi.org/10.1029/2018JD029065
Smith, R. B. (1985). On severe downslope winds. *Journal of Atmospheric Sciences*, *42*, 2597–2603. https://doi.org/10.1175/1520-0469(1985)042<2597:OSDW>2.0.CO;2
Sun, J., Burns, S. P., Delany, A. C., Oncley, S. P., Horst, T. W., & Lenschow, D. H. (2003). Heat balance in the nocturnal boundary layer during CASES-99. *Journal of Applied Meteorology*, *42*(11), 1649–1666. https://doi.org/10.1175/1520-0450(2003)042<1649:HBITNB>2.0.CO;2
Talbot, C., Bou-Zeid, E., & Smith, J. (2012). Nested mesoscale large-eddy simulations with WRF: Performance in real test cases. *Journal of Hydrometeorology*, *13*(5), 1421–1441. https://doi.org/10.1175/jhm-d-11-048.1
Werner, M. (2001). Shuttle radar topography mission (SRTM) mission overview. *Frequenz*, *55*(3–4), 75–79. https://doi.org/10.1515/FREQ.2001.55.3-4.75
Zigner, K., Carvalho, L. M. V., Jones, C., Benoit, J., Duine, G.-J., Roberts, D., et al. (2022). Wildfire risk in the complex terrain of the Santa Barbara wildland-urban interface during extreme winds. *Fire*, *5*, 138. https://doi.org/10.3390/fire5050138
Zigner, K., Carvalho, L. M. V., Peterson, S., Fujioka, F., Duine, G.-J., Jones, C., et al. (2020). Evaluating the ability of FARSITE to simulate wildfires influenced by extreme, downslope winds in Santa Barbara, California. *Fire*, *3*, 29. https://doi.org/10.3390/fire3030029